The Astrophysical Journal, 893:3 (7pp), 2020 April 10 https://doi.org/10.3847/1538-4357/ab7dc1

NuSTAR and Chandra Observations of the Galactic Center Nonthermal X-Ray Filament G0.13–0.11: A Pulsar-wind-nebula-driven Magnetic Filament

Shuo Zhang[1,2,10], Zhenlin Zhu[3,4,5], Hui Li[6], Dheeraj Pasham[6], Zhiyuan Li[5], Maïca Clavel[7], Frederick K. Baganoff[6], Kerstin Perez[8], Kaya Mori[9], and Charles J. Hailey[9]
[1] Boston University Institute for Astrophysical Research, 725 Commonwealth Avenue, Boston, MA 02215, USA; shuoz@bu.edu
[2] Bard College Physics Program, 30 Campus Road, Annandale-On-Hudson, NY 12504, USA
[3] SRON Netherlands Institute for Space Research, Sorbonnelaan 2, 3584 CA Utrecht, The Netherlands
[4] Leiden Observatory, Leiden University, Niels Bohrweg 2, 2300 RA Leiden, The Netherlands
[5] School of Astronomy and Space Science, Nanjing University, Nanjing 210046, People's Republic of China
[6] MIT Kavli Institute of Astrophysical Research, Cambridge, MA 02139, USA
[7] Institut de Planétologie et d'Astrophysique de Grenoble, Université Grenoble Alpes, CS F-40700, Grenoble, France
[8] Department of Physics and Lab of Nuclear Sciences, MIT, Cambridge, MA 02139, USA
[9] Columbia Astrophysics Laboratory, Columbia University, New York, NY 10027, USA
Received 2019 September 27; revised 2020 February 18; accepted 2020 March 6; published 2020 April 8

Abstract

One of the most unique phenomena in the Galactic center region is the existence of numerous long and narrow filamentary structures within a few hundred parsecs of Sgr A*. While more than 100 radio filaments have been revealed by MeerKAT, only about two dozen X-ray filaments have been discovered so far. In this article, we report our analysis of deep Chandra and NuSTAR observations of a nonthermal X-ray filament, G0.13–0.11, which is located adjacent to the Radio Arc. Chandra revealed a unique morphology of G0.13–0.11, which is an elongated (0.1 pc in width and 3.2 pc in length) structure slightly bent toward the Radio Arc. A pulsar candidate ($\Gamma \sim 1.4$) is detected in the middle of the filament, with a tail of diffuse nonthermal X-ray emission on one side of the filament. The filament is detected by NuSTAR up to 79 keV, with the hard X-ray centroid consistent with the pulsar candidate. We found that the X-ray intensity decays along the filament farther away from the pulsar candidate, dropping to half of its peak value 2.2 pc away. This system is most likely a pulsar wind nebula (PWN) interacting with the ambient interstellar magnetic field, where the filaments are kinetic jets from the PWN as recently proposed. The nature of this filament adds to the complex origin of X-ray filaments, which serve as powerful tools for probing local and global powerful particle accelerators in the Galactic center.

Unified Astronomy Thesaurus concepts: Galactic center (565); Interstellar filaments (842); Non-thermal radiation sources (1119)

1. Introduction

A unique and striking phenomenon in the Galactic center region is the existence of numerous nonthermal radio filaments (Yusef-Zadeh et al. 1984; Morris & Serabyn 1996; LaRosa et al. 2000). The origin and formation f these filaments have been long-standing questions for decades. Dozens of radio filaments as long as tens of parsecs have been detected by the Very Large Array within the central $\sim 2^{\circ}$ of the Galaxy, with a strong magnetic field ($\sim$1 mG) aligning along the major axis of the filaments (Yusef-Zadeh & Morris 1988; Morris & Serabyn 1996). Recent observations by the MeerKAT telescope have revealed more than 100 filaments, which seem to be associated with the newly discovered bipolar radio bubbles (Heywood et al. 2019). Thanks to polarization detection, the emission mechanism of nonthermal radio filaments has been pinned down to synchrotron emission. High-resolution JVLA observations have revealed entangled subfilaments within many radio filaments (Morris et al. 2014). These results suggest that radio filaments are magnetic structures, where a strong and highly organized magnetic field traps GeV electrons and produces synchrotron emission in the radio band (Morris et al. 2014; Zhang et al. 2014).

Similar filamentary structures, though at smaller spatial scales, have also been detected in the X-ray regime. About 30 pc long X-ray filaments have been detected so far, some of which have radio counterparts (Lu et al. 2008; Muno et al. 2008; Johnson et al. 2009; Ponti et al. 2015). A few scenarios have been proposed to explain X-ray filaments: pulsar wind nebula (PWN), supernova remnant ejecta or shocked molecular cloudlet, magnetic structure like radio filaments, and ram-pressure- or magnetic-field-confined stellar winds from massive stars. The combined diagnostic power of broadband X-ray timing, imaging, spectroscopy, and multiwavelength investigation from radio to TeV bands is the key to distinguish among the above scenarios.

Through the Sgr A* observational campaign and the Galactic center mini survey (Mori et al. 2015), NuSTAR has so far detected a total of four X-ray filaments above 10 keV: G359.95−0.04, G359.97−0.038, G359.89−0.08 (Sgr A–E), and G0.13–0.11. Except for G0.13–0.11, we have revealed the nature of the three other filaments, two of which were identified thanks to the broadband X-ray morphology and spectroscopy allowed by NuSTAR. Our limited sample of hard X-ray filaments shows interesting diversity. The three identified filaments possess different source natures: filament G359.95–0.04 is a PWN candidate (Wang et al. 2005), G359.97−0.038 is best explained by a shocked molecular cloudlet adjacent to supernova remnant Sgr A East (Nynka et al. 2015; Zhang et al. 2018), and G359.89–0.08 (Sgr A–E) is most likely a magnetic structure fed by TeV electrons (Zhang et al. 2014). The remaining question is whether other X-ray filaments would fall into any of the three above scenarios or bring

[10] NASA Einstein Fellow.

up yet other possibilities. The nature of the fourth hard X-ray filament, G0.13–0.11, may give us a clue and is thus of vital interest.

Filament G0.13–0.11 borders a bow-shaped radio protrusion from the Radio Arc, which is composed of many semi-aligned radio filaments extending up to a few tens of parsecs (Yusef-Zadeh et al. 1984). G0.13–0.11 was first discussed in Yusef-Zadeh et al. (2002), and interpreted as part of a diffuse molecular feature emitting a 6.4 keV Fe Kα line. Follow-up studies based on Chandra data show that G0.13–0.11 demonstrates a nonthermal X-ray spectrum characterized by a featureless power-law model (Wang et al. 2005). Wang et al. (2005) reported that the filament extends about 40″ (1.6 pc at the distance of 8 kpc) to the southeast from the point source CXOGCS J174621.5−285256, with an intrinsic width of 2″ (0.07 pc). The thin and long filamentary morphology with a slight curvature points to a magnetic-field-confined PWN as a likely source nature.

Recently, H.E.S.S. discovered a new Galactic plane, very-high-energy (VHE) point source, HESS J1746–285 ($l = 0.^{\circ}149$, $b = -0.^{\circ}103$), which was confirmed by MAGIC and VERITAS (Archer et al. 2016; HESS et al. 2018). This new VHE source is spatially coincident with G0.13–0.11, and thus a likely TeV counterpart of the filament.

Recent NuSTAR observations have allowed us to study the high-energy X-ray (>10 keV) emission from G0.13–0.11 and compare to its soft X-ray and γ-ray emission. We also obtained an order-of-magnitude deeper Chandra observation of G0.13–0.11, which makes it possible to reveal the fainter part of this intriguing filament. In this paper, we report analysis results based on deep observations of the filament G0.13–0.11 by both NuSTAR and Chandra. The paper is organized as follows. In Section 2, we introduce observations used in this study and the data reduction methods. Next, we present the broadband X-ray morphology of filament G0.13–0.11 in Section 3 and its X-ray spectral properties in Section 4. Then, we discuss our spectral energy distribution fitting using multiwavelength data obtained for this filament. Finally, in Section 5, we summarize our findings, and discuss the nature of this filament and its role in the Galactic center environment.

2. Observation and Data Reduction

2.1. NuSTAR

NuSTAR observed the Sgr A molecular cloud region during the 2012 Galactic center mini survey and the Galactic plane survey legacy program conducted in 2016. Filament G0.13–0.11 is captured in three of the six pointings (~25 ks exposure each) of the 2012 mini survey and in the 150 ks exposure observation in 2016. We used all four NuSTAR observations to study the high-energy X-ray emission from G0.13–0.11, as listed in Table 1.

We reduced the NuSTAR data using HEASOFT v. 6.19 and filtered events for periods of high instrumental background due to South Atlantic Anomaly passages and known bad detector pixels. Photon arrival times were corrected for onboard clock drift and precessed to the solar system barycenter using the JPL-DE200 ephemeris. For each observation, we registered the images with the brightest point sources available in individual observations, improving the astrometry to ~4″. For the three 2012 observations (obsID 40010004001, 40010005001, 40010006001), we used the data obtained by both focal plane modules FPMA and FPMB. For the 2016 observation (obsID 40202001002), G0.13–0.11 is only captured by FPMA but not FPMB. We therefore only included FPMA data for the 2016 observation.

Table 1
NuSTAR and Chandra Observations of G0.13−0.11

Instrument	Observation ID	Start Time (UTC)	Exposure (ks)
NuSTAR	40010004001	2012 Oct 15 00:31:07	24.0
NuSTAR	40010005001	2012 Oct 15 13:31:07	25.7
NuSTAR	40010006001	2012 Oct 16 05:41:07	23.5
NuSTAR	40202001002	2016 Oct 28 13:16:08	150.9
Chandra	945	2000 Jul 7 19:04:15	49.4
Chandra	14897	2013 Aug 7 16:58:16	51.2
Chandra	17236	2015 Apr 25 14:09:36	80.1
Chandra	17239	2015 Aug 19 17:21:58	80.1
Chandra	17237	2016 May 18 05:19:05	21.1
Chandra	18852	2016 May 18 20:49:44	53.1
Chandra	17240	2016 Jul 24 05:50:12	75.7
Chandra	17238	2017 Jul 17 18:44:48	66.1
Chandra	20118	2017 Jul 23 01:19:57	14.1
Chandra	17241	2017 Oct 2 18:53:53	25.1
Chandra	20807	2017 Oct 5 13:59:52	28.1
Chandra	20808	2017 Oct 8 15:37:12	27.1

To derive the NuSTAR spectrum of G0.13–0.11, we use a source region with a radius of $r = 20''$ centered on the source. Spectra from the same focal plane module are combined and then grouped with a minimum of 3σ signal-to-noise significance per data bin, except the last bin at the high-energy end for which we require a minimum of 2σ significance.

2.2. Chandra

The Galactic center region with the filament G0.13–0.11 in the field of view was observed by Chandra multiple times during 2000–2013. We selected two observations obtained in 2000 and 2013, respectively (~50 ks exposure time each), with G0.13–0.11 at an offset angle smaller than 1′ to avoid point-spread function (PSF) distortion at large offset angles. The Sgr A complex observation campaign from 2015 to 2017 (PI: Clavel), including a total of 10 observations, contributed an additional 470.6 ks exposure for this source (Table 1). In this data set, the offset angles for G0.13–0.11 are less than 3′. These 12 selected Chandra/ACIS observations add up to a total of 571.2 ks exposure for G0.13−0.11, reaching one order of magnitude deeper than the observations used in Wang et al. (2005). We processed these observations with CIAO v4.9 and the corresponding calibration files, following the procedure detailed in Zhu et al. (2019). We produced a merged event file after astrometric correction using the brightest point sources available in the observations. We used all 12 observations for source and background spectral extraction for the regions of interest.

3. Broadband X-Ray Morphology of Filament

The left panel of Figure 1 shows the 0.5–8 keV mosaic image made from all 12 Chandra observations (see Table 1) in the region around the filament G0.13–0.11. This filament is located at about 30 pc from Sgr A* on the projected plane (assuming the Galactic center at a distance of 8 kpc), in a region occupied by the giant molecular cloud G0.11–0.11. The orientation of this filament is roughly perpendicular to the Galactic plane.

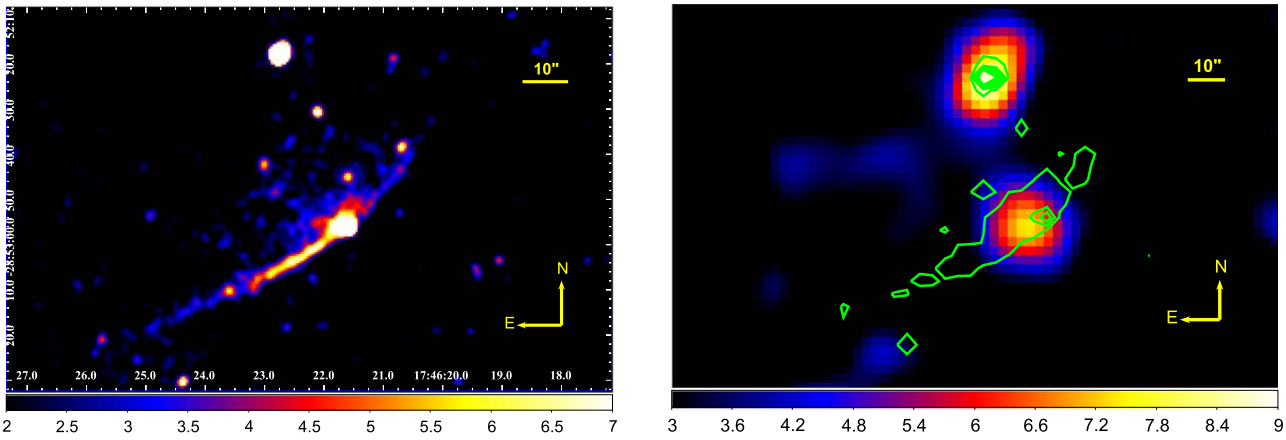

Figure 1. Left: Chandra 0.5–8 keV mosaic of the region surrounding filament G0.13−0.11, showing a thin (0.1 pc) and long (3.4 pc) structure perpendicular to the Galactic plane, with a slight curvature. The pulsar candidate CXOGCS J174621.5–285256 is located at about one-third of the filament from the northwest. Right: 10–79 keV NuSTAR mosaic of the filament region overlaid with green contours made from the 0.5–8 keV Chandra image. One point source is detected within the filament, consistent with the position of the pulsar candidate CXOGCS J174621.5–285256 as detected by Chandra. The rest of the filament is not detectable by NuSTAR. The other point source in the field is a known intermediate polar CXOUGC J174622.7–285218.

Deep Chandra observations allow us to resolve fainter parts of the filament, giving a fuller picture of its morphology. The entire filament is ∼86″ (∼3.4 pc) in length and ∼3″ (∼0.1 pc) in width (left panel of Figure 1), twice the length reported in Wang et al. (2005; ∼40″ in length and ∼2″ using about 100 ks data). The point source CXOGCS J174621.5–285256 is detected at R.A. = $17^{h}46^{m}21^{s}.62$, decl. = −28°52′56.″2, located at about one-third of the filament from the northwest. There is another bright point source detected nearby, which is CXOUGC J174622.7–285218 located at R.A. = $17^{h}46^{m}22^{s}.73$, decl. = −28°52′22.″7. It is a intermediate polar (IP) with a high temperature of $kT \sim 30$ keV, as reported in Hong et al. (2016).

The filament demonstrates a slight curvature, bending toward the northeast, i.e., the direction pointing to the Radio Arc and away from Sgr A*. The southwest side of the filament shows a sharp edge, while on the opposite side of the filament there is a fuzzy region with an excess of X-ray emission around the pulsar candidate. Such morphology suggests a picture where a pulsar, with a PWN tail, is moving toward the southwest, while hitting a highly organized magnetic structure and illuminating it with extremely relativistic electrons accelerated by the pulsar.

The right panel of Figure 1 shows the 10–79 keV mosaics of the NuSTAR observation of the region around G0.13–0.11. At the position of the filament, a point-like source coinciding with the Chandra point source is detected up to 79 keV. We overlaid the high-energy X-ray mosaic with green contours made from the 0.5–8 keV Chandra image. The centroid of the point-like NuSTAR source is ∼4″ from the Chandra position of the pulsar candidate CXOGCS J174621.5–285256, within the NuSTAR position uncertainty after astrometric correction. Therefore, the point-like X-ray source NuSTAR detected is mostly the hard X-ray counterpart of the pulsar candidate CXOGCS J174621.5–285256. The extended emission along the filament is not resolved by NuSTAR with the current data set. The nearby IP CXOUGC J174622.7–285218 is also significantly detected beyond 10 keV, due to its high temperature.

4. X-Ray Spectra and Intensity Profile of the Filament

4.1. Spectrum of the Whole Filament

For the Chandra data, we first extracted the source spectrum of the entire filament from each individual Chandra observation and the background spectrum from the selected sky region (Figure 3). We then fit the background-subtracted spectrum for each observation using a simple absorbed power-law model `tbabs*powerlaw`, which can best fit all the spectra. We found that the best-fit model parameters for all spectra are consistent among observations, suggesting no flux variability or spectral evolution for this filament from 2000 to 2017. Therefore, we next added up all the individual source spectrum and added up all the background spectrum, to derive a combined spectrum set for the filament for the following analysis. For the NuSTAR data, we extracted the source spectrum from a circular region centered on the point-like source for each individual observation. We carefully selected a partial ring region, which is in the same sky region as the Chandra background region (Figure 3), at the same distance as the NuSTAR point source from the nearby IP, to compensate for the PSF wing contamination from the IP CXOUGC J174622.7–285218. After confirming no significant source or background variability among observations, we then combined all the NuSTAR spectra as well for the following analysis.

We then jointly fit the combined background-subtracted Chandra spectrum in 2–8 keV and the NuSTAR spectrum in 3–79 keV. While the fainter part of the filament falls below the threshold of NuSTAR while Chandra detected the full signal from the filament including the point source, NuSTAR can only detect a partial signal from the filament, which is above the threshold, i.e., the point source and the brightest sections of the filaments which are not resolvable. Therefore, to evaluate this difference between the Chandra and NuSTAR detection, we introduced a constant into the models to evaluate which fraction of the whole Chandra source signal NuSTAR can detect, resulting in a model of `const*tbabs*powerlaw`. We set the constant parameter for the Chandra model to 1 and the constant for the NuSTAR model free. All the other parameters for the two spectrum sets are linked. The spectrum is featureless and can be best fit by a simple absorbed power-law model in 2–79 keV. The data do not require a spectral break or cutoff up to 79 keV, confirming the nonthermal nature. The best-fit photon index is $\Gamma = 1.7 \pm 0.2$ (error bars at 90% confidence level, same for the following). The absorption column density results in $N_{\rm H} = (1.2 \pm 0.2) \times 10^{23}$ cm^{-2} ($\chi^2_\nu = 0.9$ for d.o.f. = 207).

Table 2
Spatially Resolved Spectral Information

Source	Net Source Counts	$N_{\rm H}$ (10^{23} cm^{-2})	Γ	$F_{\rm obs(2-10\,keV)}$ (10^{-14} erg cm^{-2} s)	$L_{2-10\,\rm keV}$ (10^{32} erg s^{-1})
Point Source	825 ± 32	1.2 ± 0.3	1.4 ± 0.5	7.2 ± 0.4	8.4 ± 0.8
Fuzzy Region	2124 ± 74	1.1 ± 0.4	1.7 ± 0.5	15.1 ± 0.7	18.7 ± 1.2
Region 1	430 ± 28	1.1 ± 0.9	1.6 ± 1.1	3.5 ± 0.4	3.9 ± 0.5
Region 2	978 ± 36	1.2 ± 0.3	1.8 ± 0.3	6.7 ± 0.5	8.6 ± 0.6
Region 3[a]	377 ± 25	1.3 ± 0.8	1.9 ± 1.1	3.0 ± 0.3	3.7 ± 0.1

Note.
[a] The source regions are an $r = 2\farcs5$ circle centered on the pulsar candidate for the point source, an elliptical region to the northeast of the pulsar candidate for the fuzzy region, and $4'' \times 25''$ rectangular boxes for Regions 1–3, as shown in the upper left panel of Figure 2.

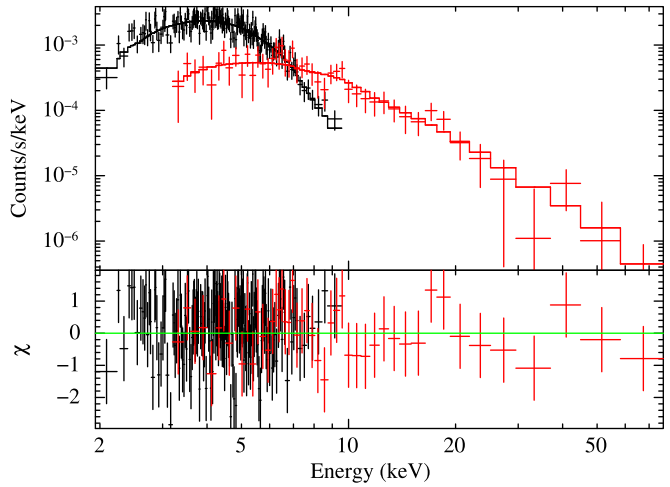

Figure 2. Joint spectral fit for the 2–8 keV Chandra spectrum and 3–79 keV NuSTAR spectrum for the entire filament. The spectra can be fit by an absorbed power-law model, with an absorption column density of $N_{\rm H} = (1.2 \pm 0.2) \times 10^{23}$ cm^{-2} and a photon index of $\Gamma = 1.7 \pm 0.2$. No spectral break of the cutoff is required by the data.

The constant for the NuSTAR model is found to be 0.55 ± .0.08, i.e., ∼55% of the entire filament is detectable by NuSTAR. The observed flux of the entire filament as detected by Chandra is $F_{2-10} = (3.1 \pm 0.1) \times 10^{-13}$ erg cm^{-2} s^{-1} in 2–10 keV and $F_{10-79} = (1.1 \pm 0.2) \times 10^{-12}$ erg cm^{-2} s^{-1} in 10– 79 keV, corresponding to luminosities of $L_{2-10} = (3.8 \pm 0.2) \times 10^{33}$ erg s^{-1} in 2–10 keV and $L_{10-79} = (9.2 \pm 0.2) \times 10^{33}$ erg s^{-1} in 10–79 keV, assuming a distance of 8 kpc.

4.2. Spatially Resolved Spectra and Intensity Profile

To investigate whether there is any spectral evolution along the filament, we studied spatially resolved spectra using all available Chandra data. We extracted spectra from five different regions within and close to the filament: an $r = 2\farcs5$ circular region centered on the pulsar candidate; the fuzzy region with excessive X-ray emission around the pulsar on the northeast side of the filament; and three $4'' \times 25''$ rectangular regions along the filament, with Region 1 on the northwest side of the pulsar candidate and Region 2 and 3 on the southeast side (see the upper-left panel of Figure 2).

The Chandra spectra from all five regions can be well fit by absorbed power-law models. The best-fit photon indices are $\Gamma = 1.4 \pm 0.5$ for the pulsar candidate, $\Gamma = 1.6 \pm 1.1$ for Region 1, $\Gamma = 1.8 \pm 0.3$ for Region 2, and $\Gamma = 1.7 \pm 1.1$ for Region 3 (Table 2). Although the best-fit values of the photon indices for the three regions ($\Gamma \sim 1.5$–1.8) along the filament are larger than the pulsar ($\Gamma \sim 1.4$), spectral softening away from the point source is not significant given the error bars. The fuzzy region to the northeast of the point source turns out to also have a featureless power-law spectrum with $\Gamma = 1.7 \pm 0.5$, which is softer than the point source and typical for a PWN. Therefore, this fuzzy region is highly likely from the PWN behind the pulsar moving toward the southwest. Figure 3 shows spectra for all five regions discussed above.

In order to derive the filament surface brightness as a function of distance to the pulsar candidate, we further divided the southern branch of the filament into eight sections along the major axis and calculated the photon flux for each section. The resultant 2–8 keV intensity profile is shown in Figure 4. The emission intensity roughly linearly decays as it gets farther away from the pulsar candidate along the filament, dropping to 50% of its peak intensity at ∼51″ (2.2 pc) from the point source. In conclusion, although significant spectral softening away from the pulsar candidate is not detected, the X-ray emission intensity drops along the filament.

5. Summary and Discussion

5.1. Origin of Filament G0.13−0.11

The filament G0.13–0.11 is located 30 pc from Sgr A* and right next to the Radio Arc. A bow-shaped radio protrusion from the radio arcs extends to the position of filament G0.13–0.11, while G0.13–0.11 itself does not have a radio counterpart. G0.13–0.11 possesses a unique X-ray morphology, with a thin and long linear structure slightly bent toward the Radio Arc. With one order of magnitude deeper observation (from 50 to 571 ks), Chandra revealed a fainter part of the filament G0.13–0.11 compared to previous work (Wang et al. 2005). The whole filament is now detected to be ∼3.2 pc in length and ∼0.1 pc in width. Based on the length of the southern branch of the filament (∼2 pc) and the synchrotron lifetime of the X-ray-emitting particles, we confirm that the magnetic-field strength along the filament is $B \leqslant 0.3$ mG as previously estimated in Wang et al. (2005). With the given magnetic-field strength, it requires the injection of TeV electrons to produce X-ray emission up to a few tens of keV as detected by NuSTAR.

A bright nonthermal X-ray point source ($\Gamma = 1.4 \pm 0.5$) resides in the middle of the filament, with a tail of nonthermal emission ($\Gamma = 1.7 \pm 0.5$) on the northeast side of the filament, the direction toward the Radio Arc. High-energy X-ray emission up to 79 keV is detected by NuSTAR from G.13−0.11, with its

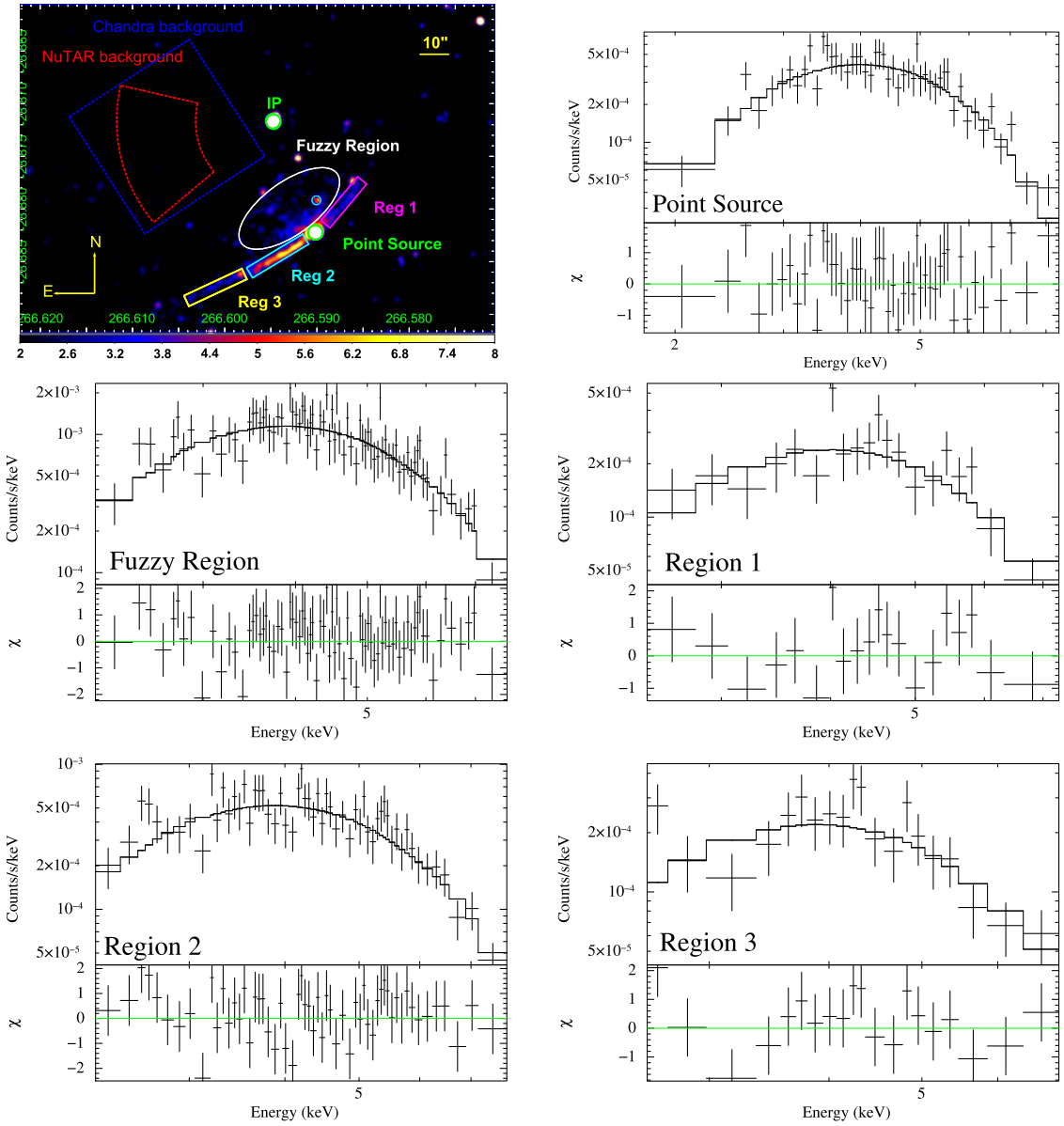

Figure 3. Spatially resolved spectra for five different regions within and around the filament. Upper left: 2–8 keV image of the filament showing the five regions from which spectra were extracted: an $r = 2\farcs5$ circular region centered on the pulsar candidate (green circle); an elliptical region on the northeast side of the filament, one point source within it excluded (white ellipse); and three $4'' \times 25''$ rectangular regions along the filament, dubbed Reg 1, Reg 2, and Reg 3. Corresponding spectra extracted from these five selected regions are shown in the other panels. The Chandra spectra from all five regions can be well fit by the absorbed power-law models. The best-fit photon indices for the different regions are listed in Table 2.

centroid consistent with the location of the point source. We found that the intensity roughly linearly decays away from the point source, dropping to half of its peak intensity at $\sim 51''$ (2.2 pc) from the point source. Furthermore, spatially resolved spectral analysis along one branch of the filament shows a trend of spectral softening along the southern branch of the filament as it gets farther away from the point source, though not significant given the error bars. If this spectral softening trend can be confirmed by future data, it will further support the scenario that there is a local particle accelerator within this filament. And the reason why the northern branch of the filament is significantly fainter than the southern branch could be due to Doppler effect, which further suggests substantial flow velocity along the filament.

Considering the nonthermal X-ray spectrum with a photon index of $\Gamma = 1.4 \pm 0.5$ and an X-ray luminosity of $L_X = (8.4 \pm 0.8) \times 10^{32}$ erg s^{-1}, the point source within the filament (CXOGCS J174621.5–285256) is most likely a young pulsar. We therefore performed a pulsation search for an $r = 20''$ region centered on the pulsar candidate in different energy bands using the NuSTAR data. A pulsation signal is not detected at a 99% confidence level with the current data. Additional exposure by the NuSTAR telescope is essential for detection of X-ray pulsation signals using a wide energy band. Nonthermal X-ray emission from the pulsar can be produced by magnetospheric emission originating from the corotating magnetosphere. The fuzzy region on the northeastern side of the filament demonstrates excessive extended nonthermal emission ($\Gamma = 1.7 \pm 0.5$). This extended emission mostly likely originates from a pulsar-driven synchrotron nebula, which suggests that the pulsar is moving toward the southwest, thus leaving its nebula tail behind.

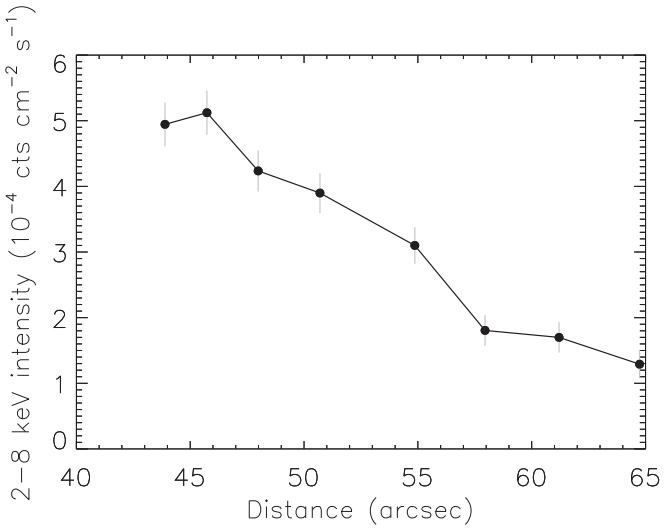

Figure 4. 2–8 keV intensity profile along the filament. The error bars are at a 1σ confidence level. The X-ray emission intensity along the filament decays as it gets farther away from the pulsar candidate, dropping 50% 2.2 pc from the pulsar.

The emission along the filament is best explained by magnetic structures fed by relativistic particles produced by the young pulsar. One possibility proposed recently for such a thin and long feature from a point source is kinetic jets or misaligned outflow from ram-pressure-confined PWNs (Barkov & Lyutikov 2019; Barkov et al. 2019), as seen from the Lighthouse PWN, the Guitar PWN, and similar systems that also demonstrate remarkably linear structures connected to a PWN (Bandiera 2008; Pavan et al. 2016). In the case of G0.13–0.11, the PWN gets confined by the magnetic field to one side of the magnetic structure, resulting in excessive nonthermal X-ray emission in the fuzzy region on the northeast side of the filament but not the other. The long and narrow features are produced through reconnection between the bow-shock PWN and ambient interstellar medium (Bykov et al. 2017; Olmi & Bucciantini 2019).

The highly organized magnetic-field structures can be preexisting, reflecting the turbulent magnetic field caused by energetic activities in the Galactic center region. When a pulsar runs into such a magnetic-field structure, the escaped TeV electrons/positrons accelerated by the pulsar magnetosphere can be confined in the magnetic-field structure, light it up, and form the jet-like features. We note that there are X-ray filaments with no obvious local particle accelerator, which calls for other mechanisms for the production of TeV electrons, as discussed in the next session.

5.2. Origin of Galactic Center Nonthermal Filaments

The nature of the radio filaments is generally better known: magnetic structures illuminated by GeV electrons. Based on recent MeerKAT results, the GeV electrons most likely come from a bursting event in the vicinity of Sgr A*, which drives a bipolar outflow and accelerated electrons at the shock front (Heywood et al. 2019), though some radio filaments might be powered by local particle accelerators such as PWNs and SNRs (Barkov & Lyutikov 2019; Barkov et al. 2019). However, the X-ray filaments seem to show more complex origins. So far, we have thoroughly studied four X-ray filaments with broadband X-ray data obtained by NuSTAR and Chandra, which lead us to conclude that one of them is a PWN; a second is a cloudlet lit up by SNR shock; a third is a magnetic structure lit up by ∼100 TeV electrons, and the fourth, i.e., G0.13–0.11, discussed in this work, is kinetic jets from a PWN. The diversity in the origin of the X-ray filaments calls for a protocol to effectively distinguish between PWN, SNR shock–cloud interaction, magnetic structure, or a combination of them. Head–tail morphology, pulsation detection, and spectral softening are evidence for PWNs; proximity to an SNR and SNR–cloud interaction signatures like an OH 1720 MHz maser and SNR ejecta emission lines would be characteristic for SNR–cloud interaction; while resolved fine structure of linear structures or even subfilaments and polarization detection demonstrating magnetic-field lines along the filament would strongly favor the magnetic structure scenario. The remaining questions are: is there a dominant mechanism for X-ray filaments? What is the relationship between X-ray and radio filaments? Do X-ray magnetic filaments have the same origin as the radio filaments? The combined diagnostic power of X-ray morphology, spectrum, timing, and a systematic comparison with high-resolution radio data like those obtained from MeerKAT would be essential to address these questions.

Among the above proposed filament natures, the magnetic structure scenario is the most intriguing, as it can explain the radio filaments and some X-ray filaments we have found. When TeV electrons/positions enter the highly organized magnetic structures, possibly with a locally enhanced magnetic field, they would produce synchrotron emission falling into the X-ray band, while GeV electrons would produce radio synchrotron emission. But the ultimate question is: where do the GeV and even TeV electrons come from? In the case discussed in this work, the filament G0.13–0.11 contains an obvious local particle accelerator within it, i.e., a pulsar, which could accelerate electrons to the required energies. However, other X-ray filaments like Sgr A–E do not contain a local accelerator within or in proximity to the filament (Zhang et al. 2014).

Below we propose a mechanism for the production of TeV electrons that can feed the X-ray nonthermal filaments within no local particle accelerator. Recent TeV γ-ray observations of the Galactic center show a strong correlation between TeV emission and molecular gas clouds, pointing to a hadronic process, where PeV protons collide into ambient gas and the proton–proton interaction producing numerous secondary particles, including neutral pions which decay into γ-ray photons (H.E.S.S. Collaboration 2016). The distribution of γ-ray emission along the Galactic plane suggests that the PeV proton accelerator (or a PeVatron) exists within the central 10 pc of the Galaxy, pointing to Sgr A* as the PeVatron candidate. Another secondary particle colliding with PeV protons within molecular clouds are relativistic electrons. According to Gabici et al. (2009), secondary electrons with energies ranging from GeV to a few hundred TeV can escape from the molecular clouds before cooling off. If the highly organized magnetic structures are close enough or are attached to the molecular clouds, they can capture the escaped ∼100 TeV electrons, which will produce synchrotron X-ray emission within the filaments. Actually, the majority of the filaments detected so far are indeed overlapping with gas clouds. The brightest X-ray filament in the Galactic center, Sgr A–E, produces X-ray emission through such a mechanism. Because there is no efficient TeV electron accelerator nearby, TeV electrons feeding Sgr A–E are most likely secondary particles from the hadronic process of PeV protons. Therefore, this subset of X-ray filaments could provide an independent approach to indirectly probe PeV protons and their accelerator. To test this hypothesis, the first necessary steps are a

thorough mapping of X-ray filaments and the discovery of more filaments using the next-generation X-ray telescope with high throughput, high spatial resolution, and polarization detection, like Athena, IXPE, and eXTP.

This work made use of data from the NuSTAR and Chandra missions. We thank both the NuSTAR and Chandra Operations, Software, and Calibration teams for support with the execution and analysis of these observations. S.Z. acknowledges support from NASA through the NASA Hubble Fellowship grant # HST-HF2-51450.001-A awarded by the Space Telescope Science Institute, which is operated by the Association of Universities for Research in Astronomy, Inc., for NASA. M.C. acknowledges financial support from the French National Research Agency in the framework of the "Investissements d'avenir" program (ANR-15-IDEX-02) and from CNES.

ORCID iDs

Shuo Zhang https://orcid.org/0000-0002-2967-790X
Zhiyuan Li https://orcid.org/0000-0003-0355-6437
Maïca Clavel https://orcid.org/0000-0003-0724-2742
Kerstin Perez https://orcid.org/0000-0002-6404-4737
Kaya Mori https://orcid.org/0000-0002-9709-5389

References

Archer, A., Benbow, W., Bird, R., et al. 2016, ApJ, 821, 129
Bandiera, R. 2008, A&A, 490, L3
Barkov, M. V., & Lyutikov, M. 2019, MNRAS, 489, L28
Barkov, M. V., Lyutikov, M., Klingler, N., & Bordas, P. 2019, MNRAS, 485, 2041
Bykov, A. M., Amato, E., Petrov, A. E., Krassilchtchikov, A. M., & Levenfish, K. P. 2017, SSRv, 207, 235
Gabici, S., Aharonian, F. A., & Casanova, S. 2009, MNRAS, 396, 1629
H.E.S.S. Collaboration 2016, Natur, 531, 476
H.E.S.S. Collaboration, Abdalla, H., Abramowski, A., et al. 2018, A&A, 612, A9
Heywood, I., Camilo, F., Cotton, W. D., et al. 2019, Natur, 573, 235
Hong, J., Mori, K., Hailey, C. J., et al. 2016, ApJ, 825, 132
Johnson, S. P., Dong, H., & Wang, Q. D. 2009, MNRAS, 399, 1429
LaRosa, T. N., Kassim, N. E., Lazio, T. J. W., & Hyman, S. D. 2000, AJ, 119, 207
Lu, F. J., Yuan, T. T., & Lou, Y.-Q. 2008, ApJ, 673, 915
Mori, K., Hailey, C. J., Krivonos, R., et al. 2015, ApJ, 814, 94
Morris, M., & Serabyn, E. 1996, ARA&A, 34, 645
Morris, M. R., Zhao, J.-H., & Goss, W. M. 2014, in IAU Symp. 303, The Galactic Center: Feeding and Feedback in a Normal Galactic Nucleus, ed. L. O. Sjouwerman, C. C. Lang, & J. Ott (Cambridge: Cambridge Univ. Press), 369
Muno, M. P., Baganoff, F. K., Brandt, W. N., et al. 2008, ApJ, 673, 251
Nynka, M., Hailey, C. J., Zhang, S., et al. 2015, ApJ, 800, 119
Olmi, B., & Bucciantini, N. 2019, MNRAS, 490, 3608
Pavan, L., Pühlhofer, G., Bordas, P., et al. 2016, A&A, 591, A91
Ponti, G., Morris, M. R., Terrier, R., et al. 2015, MNRAS, 453, 172
Wang, Q. D., Lu, F. J., & Gotthelf, E. V. 2005, MNRAS, 367, 937
Yusef-Zadeh, F., Law, C., & Wardle, M. 2002, ApJL, 568, L121
Yusef-Zadeh, F., & Morris, M. 1988, ApJ, 329, 729
Yusef-Zadeh, F., Morris, M., & Chance, D. 1984, Natur, 310, 557
Zhang, S., Hailey, C. J., Baganoff, F. K., et al. 2014, ApJ, 784, 6
Zhang, S., Tang, X., Zhang, X., et al. 2018, ApJ, 859, 141
Zhu, Z., Li, Z., Morris, M. R., Zhang, S., & Liu, S. 2019, ApJ, 875, 44